Multifunctional green composites based on plasma-activated and GO-coated dwarf palm fibers

Andrea Maio and Roberto Scaffaro*

Department of Engineering-Research Unit INSTM, University of Palermo, Viale delle Scienze, 90128 Palermo, Italy

*Corresponding author: roberto.scaffaro@unipa.it

Abstract

In this work, we propose a green method for decorating natural fibers derived from dwarf palm waste with graphene oxide (GO) sheets. In detail, plasma-treatment was used to activate fiber surface for the subsequent GO-coating, which was performed in water. Poly(butylene adipate-co-terephthalate) (PBAT)-based composites incorporating 50% of either raw, plasma-modified or hybrid fibers were prepared by compression moulding and thoroughly analysed to investigate the processing-structure-properties relationships of these systems. The outcomes reveal that combining plasma treatment and GO coating enables fabricating green composites with significantly improved mechanical performance (stiffness and tensile strength increments of up to 500% and 300%, respectively) and electrical conductivity on the order of 10^{-6} S/m.

Keywords: A: Natural fibers; Graphene; Hybrid; Polymer-matrix composites (PMCs).

1. Introduction

Bioplastics play a significant role in modern society due to their lightweight nature and sustainability[1]. However, their limited mechanical robustness, durability, and cost-effectiveness have hindered their widespread industrial adoption. To address these challenges, incorporating inexpensive natural fillers in place of a significant portion of bioplastics has emerged as a promising alternative [2,3]. This not only reduces manufacturing costs but also valorizes agro-waste [4,5]. In fact, considering that about 181.5 billion of tonnes of biomass are annually produced [6], the appropriate valorisation of non-edible biomass provides effective waste management solution, which may prevent its accumulation, thus transforming a problem into valuable by-products [7–12]. While significant progress has been made in the fabrication of green composites, the development of strategies to create smart and functional materials from natural sources remains uncommon. Current approaches predominantly focus on using nanocellulose or lignin as fillers [13–15]. However, the exploration of utilizing raw lignocellulosic fibers

instead of their nano-sized constituents offers a valuable alternative for faster and greener manufacturing processes, especially when considering that acid, alkaline, and other chemical treatments usually involved to prepare nanocellulose and lignin, seriously affect their economic and environmental sustainability [7,16–18]. The key challenge in developing high-performance green composites with natural fibers lies in establishing strong interfacial interactions between the fiber and matrix without the need for chemicals or complex multi-step protocols[19].

Utilizing natural fibers as a substrate for multifunctional nanoparticles holds promise in the development of affordable and eco-friendly advanced fibers, as surface chemistry plays a crucial role in determining their properties. Previous research has demonstrated that core-shell structures with graphene armor exhibit exceptional mechanical robustness [20]. Furthermore, the unique morpho-chemistry of graphene oxide (GO) foils, characterized by a crumpled and rough surface abundant in oxygenated moieties and aromatic domains, provides an active platform for polymer chain anchoring [21]. While many studies have explored the wrapping of GO sheets around carbon fibers to enhance the interphase of carbon fiber-reinforced polymers (CFRPs) [22–24], there is a lack of systematic research on GO-coating of natural fibers for bioplastic reinforcement, since only recently few pioneering studies are starting to emerge [25–33]. In addition to improving mechanical properties, GO-coating of natural fibers offers the intriguing possibility of transforming their electrical characteristics from insulator to semiconductor - or even conductor - via the partial or total reduction of GO [32,34–36]. This opens up opportunities for achieving a percolation network of conductive nanoparticles by leveraging a percolated network of natural fibers as a substrate for nanoparticle deposition. Such a strategy could facilitate the development of electrically conductive materials with lower amounts of costly nanoparticles and higher utilization of waste bio-sources. Beyond this, multifunctional materials containing nanocarbon-coated waste biomass fibers might find application as cheap multifunctional materials in many emerging areas in which polymer composites containing graphene or other nanoparticles are typically used, including electromagnetic and or micro-wave absorption, strain sensors, supercapacitors, triboelectric nano-generator sensors, and so on [37–46].

Unfortunately, while it is relatively simple to decorate carbon fibers with GO, by exploiting the strong aromatic interactions between the two carbonaceous components, coating natural fibers with GO poses additional challenges compared to carbon fibers due to the heterogeneity of lignocellulosic materials and the limited accessibility of -OH moieties [20]. Lignocellulosic materials, including natural fibers, possess a hierarchical structure comprising cellulose fibrils embedded in a matrix of lignin and hemicellulose.

Notably, the external walls of natural fibers consist of hemicellulose-coated lignin [47]. Understanding and addressing these complexities are crucial for successful GO coating of natural fibers. To establish a robust affinity between lignocellulosic fibers and GO sheets, two distinct approaches can be pursued. Firstly, activating the surface of hemicellulose by introducing emerging epoxy and hydroxyl moieties is expected to facilitate strong interactions between the natural fibers and the oxygenated functional groups present in GO. Alternatively, selectively removing hemicellulose from the fibers can increase the surface concentration of lignin. This strategy offers another viable route to improve the affinity of natural fibers for the aromatic domains of GO. According to the scientific literature, both of these strategies can be implemented in a non-toxic and efficient manner through plasma reactions, by carefully adjusting key operating parameters such as exposure time and plasma power [48–53].

In this study, we present a sustainable processing approach that combines plasma treatments and an aqueous processing step to effectively coat dwarf palm fibers with graphene oxide nanosheets. Subsequently, the hybrid fibers obtained were assessed for their potential to reinforce a poly(butylene adipate-co-terephthalate) (PBAT) matrix. Indeed, PBAT is a biodegradable copolymer that comprises aliphatic and aromatic domains linked by C=O bonds. Its structure may offer the advantage of facilitating interactions with both the oxygenated functional groups and the aromatic domains present in GO, making it a suitable matrix for incorporating the modified fibers. On the other hand, dwarf palm, belonging to *Chamaerops humilis L.*, is a non-edible plant that presents diffusion control challenges due to its invasive nature, which harms native Mediterranean flora. It is possible to derive fibers from its dead wastes that are particularly rich in lignin (35 %) and cellulose (40%) [54], thus being potentially suitable for interacting with both GO and PBAT towards the construction of green yet multifunctional materials. Integrating 50% of a waste biomass such as dwarf palm in a composite material means halving raw material cost, while reducing environmental impact and energy consumption. Moreover, using endemic biomass waste may offer additional financial incentives or regulatory benefits, given the fact that the resulting green materials may gain a competitive edge in certain markets, driven by the recent zero-waste and circular economy guidelines.

2. Materials and methods

2.1 Materials and processing

PBAT selected for this study was a sample of Ecoflex® F Blend C1200 purchased from BASF (Germany), having the following characteristics: melt flow index = 2.7–4.9 g/10 min (at 190 °C and 2.16

kg), density=1.25–1.27 g/cm^3, melting temperature=110–120 °C. Agro-waste of *Chamaerops humilis* (CH) samples, collected in the western seacoast of Palermo, were thoroughly washed to remove impurities. Stalks (CHS) were isolated from leaves, and successively grounded and sieved in order to obtain fibers with minimum length equal to 4 mm, which results in an aspect ratio (L/D)= 40.

The selected GO sample used in this study was synthesized in our laboratories and has been employed in our previous research [55,56]. It is a partially oxidized GO variant with 55% aromatic sp^2 domains and a C/O ratio of 7:3. The GO material consists of few-layered lamellae with lateral dimensions ranging from 5 to 20 µm, a thickness of 0.8 nm, and an interlamellar spacing of 0.95 nm. More details about synthesis and characterizations are provided in SI (Fig. S1 a-d) and available elsewhere [55,56]. This specific GO batch was chosen based on its demonstrated electroactivity and its established affinity to other biodegradable polyesters [55].

The plasma reactor used for the surface treatment is a Tucano Gambetti apparatus, equipped with a high vacuum-pump (Pfeiffer). The cylindrical chamber (diameter = 150 mm, length = 330 mm) has a volume of approximately 5.5 dm^3. The dark shield electrode and the power supply (RF=13.56 MHz, 200 W) are placed at the top of the chamber. The flow of the air takes place automatically at vacuum level and power programmed in the recipes with two mass flow-controllers, and it is controlled by a microcomputer. In this case, air flow was set to 10 sccm, the vacuum level was $2 \cdot 10^{-4}$ bar and the vacuum was stabilized for 5 s prior to the process gas inlet.

After the gas inlet, the chamber pressure reached approximately 0.5 mbar, and the treatment was carried out at different power and time settings, with adjustments made to minimize reverse bias. In accordance with previous research [48], two conditions were employed: "Type 1" plasma treatment was performed at 100 W for 2 minutes, while "Type 2" treatment was carried out at 60 W for 10 minutes. The fibers resulting from these plasma modifications were designated as p1-CHS and p2-CHS, respectively. As provided in **Figure 1a**, to prepare a batch of GO-coated fibers, either raw or plasma-treated fibers were added to an aqueous suspension of GO (1 g/L, 125 mL). The mixture was sonicated in an ice bath for 30 minutes and then vigorously stirred for 4 hours. Subsequently, each dispersion containing GO and natural fibers was transferred to a crystallizer, and the temperature was raised to 180 °C to facilitate solvent evaporation and the consolidation of the GO-coated fibers. During the thermal treatment, the color of the fibers changed from yellow/light brown to dark grey (see digital photographs in the same figure), indicating the partial reduction of GO. The resulting coated fibers, referred to as GO@CHS, GO@p1-

CHS, and GO@p2-CHS, were stored overnight in a vacuum-oven at 120 °C before being processed with PBAT.

Figure 1b provides the pictorial description of the typical procedure followed to obtain green composites. PBAT sheets, previously prepared by compression-moulding (T= 145 °C for 2 minutes) by using a Carver (USA) laboratory press, were used to form a sandwich incorporating an appropriate amount of fibers, displaced by a hand lay-up process, until achieving a total coverage of the mold volume. As depicted in **Figure 1b**, both polymer sheets extended beyond the mold dimensions. During the hot-pressing stage (155 °C, 4 minutes, 7 tons), some of the PBAT was forced into the voids between the fibers, while the excess polymer flowed out and was trimmed once the material rapidly cooled to room temperature. This technique allows preparing composites with extremely high loading levels.

The resulting materials were weighed, and their composition was determined by subtracting the pre-weighed amount of fibers from the total weight of the composite after removing the excess polymer.

Characterization techniques

The morphology of both the starting components and green composites was examined using scanning electron microscopy (SEM) imaging performed with a Phenom Pro X instrument from Thermo Fisher Scientific, USA.

The density measurements were conducted using a Thermo Pycnomatic Helium Pycnometer (Pycnomatic ATC, Thermo Fisher, USA) with 99.99% pure helium gas. Each sample was subjected to at least five measurements at a temperature of 20 °C.

The GO content of hybrid fibers was determined according to our previous studies [54,57–59], as follows (Equation 1):

$$GO\ content\ (\%) = \frac{\rho_{GO-coated\ fibre} - \rho_{fibre}}{\rho_{GO} - \rho_{fibre}} \qquad (1)$$

Where $\rho_{GO-coated\ fibre}$, ρ_{GO} and ρ_{fibre} respectively refer to the real densities of GO-coated fibers, GO and CHS fibers.

In order to determine the degree of porosity (%) for each material, the following relationship was used (Equation 2):

$$Porosity\ (\%) = \left(1 - \frac{\rho_a}{\rho_r}\right) \times 100 \qquad (2)$$

where ρ_a and ρ_r refer to apparent and real densities, respectively.

Attenuated total reflection Fourier transform infrared (FT-IR/ATR) measurements were performed using a FT-IR/NIR Spectrum 400 spectrophotometer (PerkinElmer, Waltham, MA, U.S.A.) in the spectral range 4000-450 cm^{-1}. Micro-Raman spectroscopy was performed in the range 1000–2000 cm^{-1} by means of a Renishaw InVia instrument (Renishaw) with diode laser excitation at 633 nm and spectral resolution equal to 1 cm^{-1}.

Tensile tests were performed using an Instron 3365 dynamometer (Instron, USA) onto specimens having a thickness of approximately 650-800 µm. In accordance with the ISO 527-3 standard, the tests were carried out with an initial crosshead speed of 1 mm/min for the first 3 minutes, followed by increased crosshead speed of 100 mm/min until specimen failure. Each experimental run included at least 8 replicates, and salient data such as elastic modulus (E), tensile strength (TS), and elongation at break (EB) were reported as mean values with corresponding standard deviations.

Electrical measurements were performed using a Keithley 2440 source meter. Prior to the experiments, square-shaped samples (10 mm x 10 mm, ~0.7 mm thick) were placed between two copper electrodes. Current intensity (I)-voltage (V) curves were acquired in the range 0-10 Volt (integration time = 0.5 s; pass=100 mV), and the conductance, i.e. the reciprocal of resistance (1/R), was measured as the slope of the curves in their linear zone. Conductivity (σ) was then calculated by Equation (3):

$$\sigma = \frac{L}{S\,R} \qquad (3)$$

Where L and S are, respectively, the thickness and surface area of specimens.

3. Results and discussion

GO-coating of neat and plasma-treated CHS fibers was verified by integrating morphological and spectroscopic analyses. SEM analysis of the samples is provided in **Figs 2-3**.

Raw CHS fibers (Fig. 2a-a') exhibit the characteristic features of dwarf palm stalks, with a densely packed structure consisting of a bundle of aligned fibrils held together by a hemicellulose matrix.

However, following the sequential treatments of washing, grinding, and ultrasonication, CHS fibers underwent a morphological change. The resulting structure is heterogeneous, featuring aligned bundles of

fibers (Fig. S2a), porous architectures (Fig. S2 a-b), eventually covered by wrinkled zones (Fig. S2 c), with embedded silica nanoparticles (Fig. S2 d).

In the analysis of p1-CHS fibers (Fig. 2b-b'), it was observed that the treatment did not result in prominent structural changes. However, specific regions exhibited partial etching of the hemicellulose matrix and enhanced visibility of the bundle of aligned fibrils. Conversely, in p2-CHS fibers (Fig. 2c-c'), extended plasma exposure led to more substantial modification to the fiber structure, characterized by severe ablation of the hemicellulose matrix and the formation of a skeleton likely composed of lignin and cellulose[53]. Notably, both plasma treatments induced modifications that were minimally or moderately significant compared to those caused by grinding and purification (refer to Figs. S2 a-d). Essentially, the differences observed between samples are similar to variations within the same sample, attributed to the inherent heterogeneity of the lignocellulosic fibers and the variegated modification incurred during washing, grinding, and ultrasonication.

Additionally, it is noteworthy that certain regions of CHS and plasma-treated fibers, especially after sonication, exhibit a morphology similar to that of graphene oxide (GO) flakes (see Fig. S1 a-b), particularly when these flakes are stacked together.

Figure 3 provides micrographs of GO@CHS (Fig. 3a-a'), GO@p1-CHS (Fig. 3b-b'), and GO@p2-CHS (Fig. 3c-c') at two different magnifications. Despite the initial differences among the three CHS samples and their intrinsic heterogeneity, the coating with GO resulted in similar and uniform fiber morphology, characterized by an extremely rough texture.

Therefore, although the notable grey color change – from light brown/yellowish to dark grey – exhibited by the fibers post-coating (see again digital photographs of the fibre samples in **Figure 1**) suggests the plausible presence of graphene oxide (GO) on their surface, identifying GO via SEM imaging is challenging due to the visual resemblance between the fibers and GO. Nevertheless, in certain instances, it becomes feasible to observe exfoliated GO layers emerging from the fiber surface, as depicted in Figure S3.

EDAX mapping (see SI, Tab. S1) performed on the samples put in evidence that both CHS fibers and GO are mainly constituted of C and O elements, with this feature rendering once again extremely difficult to assess the existence and the extent of surface coating. However, it is worth noting that CHS fibers (Fig. S4) display the presence of Si, due to the fact that such plants, growing in the proximity of the sea are

capable of integrating significant amounts of silica nanoparticles embedded within the plant structure [60]. After GO-coating, the amount of silica tend to decrease, because it is covered by the presence of GO sheets. Furthermore, the homogeneous presence of GO can be indirectly confirmed by the presence of sulphur atoms(Figs. S5-S7), due to the small amount of sulfonated groups onto GO sheets as a result of H_2SO_4 used for oxidizing graphite to GO [61].

Figure 4 presents the results of FTIR/ATR spectroscopy for both raw and plasma-treated CHS fibers, while **Table 1** summarizes the main peak assignments of the spectral modes, allowing for a clear identification of the structural components present in lignocellulosic fibers, including hemicellulose, cellulose, and lignin. FTIR/ATR spectrum of raw CHS fibers displays the typical set of absorption modes associated with hemicellulose, lignin, and cellulose, which are the predominant constituents of lignocellulosic materials (**Table 1**) [49,62,63]. Spectra of plasma-treated samples show some differences, including a redistribution of the relative intensity ratios between the various bands and, in some cases, also the formation of emergent modes.

In more detail, when fibers were exposed to short-duration, high-power air plasma (p1-treatment), there was an observed increase in the bands associated with hemicellulose and pectin, accompanied by the emergence of a peak at around 1150 cm^{-1}, close to the C-O stretching of the acetyl group (refer to **Fig. 4** and **Tab. 1** for further details). These changes suggest that this type of plasma treatment primarily modifies the surface of hemicellulose and pectin, which are components of the outer walls of the fibers. This hypothesis could explain the lack of significant changes in fiber morphology observed by SEM.

On the other hand, fibers treated with prolonged exposure to low-power plasma (p2-treatment) showed an increase in the signals associated with cellulose and particularly lignin, which became more pronounced compared to hemicellulose. By comparing these results with the etching events observed during SEM, it can be inferred that this type of plasma treatment may have selectively removed the hemicellulose matrix, resulting in a relative increase in the amount of surface lignin. This finding is consistent with existing literature, which indicates that air plasma has limited effectiveness in removing lignin from natural fibers [49].

Plasma-treated fibers exhibited a higher adsorption capacity for GO compared to raw CHS, indicating an enhanced extent of GO loading. **Table 2** presents the weight content of GO in the three fiber samples, ranging from 1.7% to 2.1%, suggesting that increased roughness and surface activation improved the

efficiency of GO loading. A comparison between the two treatment types reveals that air plasma treatment at 100 W for 2 minutes demonstrates slightly greater effectiveness than treatment at 60 W for 10 minutes. In other words, activating hemicellulose through the p1-treatment is supposed to promote stronger interactions with the oxygen moieties of GO, while the partial ablation of hemicellulose and subsequent surface exposure of lignin by the p2-treatment might have facilitated aromatic interactions. Both approaches result in a significant increase in GO loading on the fiber surface, owing to the exceptional versatility of GO, which possesses a double honeycomb structure composed of sp^2 and sp^3 carbon domains.

Aiming to assess eventual differences in the chemical structure of the three samples, FTIR/ATR spectroscopy was used. In **Fig. 5a-c** there are reported the representative spectra of the three CHS samples before and after GO-coating, along with that of GO as a reference plot. As one can see, starting materials present similar key-modes, including the broad band in the spectral range 3600-3000 cm^{-1} (ascribed to OH moieties), a band bearing a double peak centred at 2916 and 2849 cm^{-1} attributable to C-H alkyl chains. In the range 1750-1500 cm^{-1}, CHS displays a well-defined peak located at 1734 cm^{-1} due to C=O stretching of ester bonds and an overlapped band characterized by a prominent peak at 1594 cm^{-1} with a shoulder around 1645 cm^{-1}, ascribed to C=O stretching conjugated to the aromatic ring of lignin fraction of CHS. In the same spectral region, GO displays its typical double-peak band with signals at 1713 cm^{-1} and 1615 cm^{-1} that are respectively ascribed to C=O stretching of carboxylic acid moieties and aromatic C=C skeleton of the graphenic lattice of GO. In the wavenumber range 1510-1200 cm^{-1}, GO shows a bunch of overlapped signals, while CHS displays distinct modes centred at 1508 cm^{-1} (peculiar of lignin) 1461 cm^{-1} (-CH_2- symmetric stretching), 1422 cm^{-1}, 1368 cm^{-1} (alkene stretching), 1317 cm^{-1} (-CH_2 in plane-angular vibration, key-mode of crystalline cellulose), and 1239 cm^{-1}. After coating, the fibers present an extremely more intense absorption in the range 3600-3000 cm^{-1}. Among the samples, GO@p1-CHS showed the highest intensity, followed by GO@p2-CHS, whereas GO@CHS displayed the lowest signal. Furthermore, in the spectra of samples containing plasma-treated fibers, such broad band displayed an emergent signal located at 3350 cm^{-1}, beyond the aforementioned peak at 3273 cm^{-1} of natural fibres (OH stretching, see again **Table 1**). Likewise, this occurrence could be due to the larger extent of H-bonding between oxygenated moieties of GO and plasma-activated lignocellulosic fibres. A careful analysis of double-peak band (2916-2849 cm^{-1}) pointed out significant differences between GO@CHS and GO-decorated plasma-treated fibers. In the former case, the two signals proved to overlap to each other, becoming much similar to the spectral features of neat GO, in the latter case, instead, a

hybrid band arises from recombination of the modes of starting components. Similar considerations can be drawn by analysing the features of the other spectral regions, such as for example those of carbonyl (1800-1650 cm^{-1}), C-H (1461-1300 cm^{-1}), C-O (below 1250 cm^{-1}).

Hence, to further confirm the presence of GO onto the surface of functionalized fibers, Raman spectroscopy was used, because this technique is highly sensitive onto the carbonaceous structure of GO, while being scarcely or not sensitive to lignocellulosic fibers[32,64]. **Figure 6a-c** provides the representative spectra of CHS, p1-CHS, p2-CHS before and after GO-coating, along with those of GO as a reference plot. Raman spectra of all the GO-coated fibers clearly show the characteristic D-band (around 1340 cm^{-1}) and G-band (around 1580 cm^{-1}) of GO, which are not present in the spectra of CHS, p1-CHS, and p2-CHS. Noteworthy, ID/IG ratios, peak positions and eventually FWHM of D- and G-bands proved to vary, indicating the strong interaction between GO and the substrate, or partial reduction of GO[32,57,58].

The mechanical behaviour of the composites achieved incorporating 50 wt.% of different samples of CHS fibres was analysed by tensile tests and the results are provided in **Figure 7** and **Table 3**, respectively reporting representative stress-strain curves and the salient data collected.

Except for the composites containing GO@CHS, all the other materials exhibit a ductile mode of fracture. It is worth noting that after yield, the curves show a gradually declining trend, initially more steady and then slower, with an almost plateau-like pattern until failure. This characteristic indicates the occurrence of necking and fraying events, resulting in significant reduction in the resistant surface.

Figure 7b offers a comprehensive overview of the variations in the salient mechanical properties of the composites following each treatment, including plasma activation and/or GO-coating of fibers, in comparison to the composite with untreated CHS.

While all the treatments applied to CHS fibers resulted in remarkable yet different increases in stiffness for the corresponding composites, the impact on tensile strength (TS), elongation at break (EB), and toughness varied depending on the specific treatment. For instance, when applying plasma treatment or GO coating to the fibers individually, there were observed effects of stiffening and strengthening, albeit at the cost of deformability and toughness. More in details, the quantitative analysis of data provided in Table 3 and Fig. 7b, put into evidence that p1-treatment and p2-treatment resulted in a doubling and an almost tripling of the elastic moduli, respectively, in comparison to the composite containing raw fibers.

The TS values remained unchanged, while deformability exhibited variations based on the type of plasma treatment. Specifically, p1-treatment resulted in a doubling of the elongation at break (EB), while p2-treatment had a negligible impact on deformability. Noteworthy, composites incorporating GO@CHS demonstrated further improvements in both E and TS, while experiencing a 40% reduction in EB. Ultimately, the toughness of materials loaded with either plasma-treated or GO-coated fibers was found to be lower than that of composites containing raw fibers.

Significantly, the combination of the two treatments resulted in a remarkable improvement in all the mechanical properties. It is worth noting that composites containing GO@p1-CHS showed the most remarkable enhancements in terms of stiffness, strength, stretchability, and toughness, with relative increments of up to 500%, 250%, 200%, and 180%, respectively. On the other hand, composites containing GO@p2-CHS exhibited slightly lower mechanical performance but still outperformed the remaining samples.

Based on these results, an intriguing interaction between the type of plasma treatment and GO-coating could be inferred. Specifically, composites incorporating p2-CHS demonstrated superior mechanical robustness compared to those containing p1-CHS. Conversely, a reversed trend was observed in the case of GO-coated plasma-treated fibers, with GO@p1-CHS exhibiting greater mechanical reinforcement than GO@p2-CHS. This suggests that the p2-type treatment may be more suitable for promoting interactions between fibers and GO, whereas the p1-treatment likely enables stronger interactions between fibers and the polymer. To confirm these hypotheses, a thorough analysis of the morphology of tensile fractured surfaces was performed.

Figure 8 provides the SEM micrographs at different magnifications of composites containing CHS (a-a'), p1-CHS (b-b'), and p2-CHS (c-c'), acquired in two different specimen positions for each sample. In all cases, the typical features of a ductile fracture are clearly identifiable, in full agreement with the previously discussed stress-strain behaviour. This feature can be obviously ascribed to the well-known ductility of neat polymer (see Fig. S8). Interfacial adhesion in the PBAT-CHS composite proved to be adequate, although some voids were observed.

Notably, plasma-treated fibers exhibited a significantly stronger interaction with PBAT. This is evident from the discernible breakage of the dwarf palm microfibrils, indicating that the interfacial adhesion was so robust that specimen failure occurred due to the fracture of either the fibers or the matrix.

The morphology of composites containing GO-decorated fibers was carried out to assess the durability of the GO-coating, specifically the adhesion between GO and the fibers, as well as the interfacial adhesion between these decorated fibers and the surrounding polymer matrix. **Figs 9a-c** respectively report the micrographs of PBAT-based composites loaded with GO@CHS, GO@p1-CHS, and GO@p2-CHS, acquired in two different positions for each sample and eventually at different magnifications.

PBAT-GO@CHS (Fig. 9a) exhibits a smooth surface, consistent with a brittle mode of tensile fracture, aligning with mechanical test results. Additionally, the presence of voids and fiber pull-out (bottom panel of Fig. 9a) suggests weak interactions between GO and untreated CHS fibers. This led to the detachment and aggregation of GO sheets (highlighted by the red circle), ultimately deteriorating the interphase. In contrast, the composites containing GO@p1-CHS (Figure 9b) and GO@p2-CHS (Figure 9c) displayed the typical rough surface of ductile materials, with the hybrid fibers showing a robust and durable GO-coating (see top panels). These composites exhibited a prominently deformed polymer phase that strongly adhered to the hybrid fibers (highlighted by red circles), also demonstrating a strong multiple interphase, as evidenced in the bottom panels of **Figs** 9**b-c**.

Porosity is a critical factor influencing the mechanical behaviour of composite materials, its related results are reported in **Table 4**. Undoubtedly, the porous nature of fibers may significantly affect the densification process of composites, particularly considering that CHS fibers exhibit a porosity level of 45-50%. The entry of PBAT macromolecules into the internal voids can be influenced by various factors, including the total volume of pores, their dimensions, and availability.

Composites containing both CHS and p1-CHS show similar levels of porosity, typically about 15%. This indicates that at least half of the internal lumens are filled with polymer inclusions. With p2-CHS, the partial ablation of the surface walls enhances the formation of the so-called “intraphase structures”, allowing PBAT chains to occupy empty spaces within the fibers. Consequently, denser composites are achieved.

However, the presence of GO sheets on the fiber surface tends to hinder the penetration of macromolecules inside the fibers, especially for the samples decorated with stronger chemical bonds and thicker GO coatings. Consequently, the composites containing GO-coated fibers exhibit lower density, especially those containing GO@p1-CHS and GO@p2-CHS, which showed the highest porosity values.

In light of this latter aspect, the enhancements in mechanical reinforcement observed in these latter systems are even more outstanding.

The electrical properties of the samples were evaluated, and **Figure 10a** illustrates the current- voltage (I-V) characteristics of the composites containing GO-coated fibers, along with a reference composite prepared with 1 wt.% GO. Furthermore, Figure **10b** presents the I-V characteristics of a specimen composed solely of GO, thermally treated under the same conditions as the composites, serving as an additional control. It is important to note that neat PBAT and green composites consisting solely of fibers exhibited no discernible current flow, falling below the detection limit of the instrument.

All the samples demonstrate non-linear I-V characteristics, with this behavior being particularly prominent in the composites. Conversely, the GO reference sample exhibits a nearly linear curve, consistent with findings reported in other scientific studies [55].

Nonlinear I-V behavior has been thoroughly studied in polymer composites containing graphene or other conductive particles. It can be influenced by several factors related to the composite structure, the electrical properties of components, and the electrical transport mechanisms involved, and so on [55,65,66]. At low applied voltages, the current flows through the polymer matrix, which typically has extremely low conductivity [55,65,66]. However, as the voltage increases, the current starts to flow preferentially through the interconnected graphene flakes, resulting in a nonlinear rise in current [55,65,66]. However, beyond a specific voltage threshold, the current exhibits a substantially linear increase with applied voltage, with the slope representing the electrical conductance (1/R).

By examining the curves presented in **Figure 10**, one can qualitatively assess the electrical conductivity trend. The corresponding electrical conductivity (σ_0) values are provided in **Table 5**.

Expectedly, thermally treated GO demonstrates the highest electrical conductivity, reaching approximately 10^{-3} S/m. In contrast, the composite incorporating 1 wt.% GO in a PBAT matrix (PBAT+1%GO) exhibits the weakest electrical response, with a conductivity of about 10^{-11} S/m. This finding suggests that the GO amounts used in this study are below the percolation threshold. Interestingly, despite containing a GO content below or similar to 1%, the composites incorporating GO@CHS, GO@p1-CHS, and GO@p2-CHS exhibit higher current flows (in the order of 10^{-6} S/m).

To explain this counterintuitive behavior, it is important to consider that the relatively low conductivity of GO, coupled with its tendency to self-aggregate when melt-compounded with polymers, often hinders the formation of continuous conductive pathways at low loading levels. To address this challenge, various strategies employing steric hindrance and nanoparticle confinement have been proposed to achieve percolation thresholds at lower filler contents.

One effective approach involves creating a co-continuous blend with selective filler localization in one phase or at the interface. This technique has demonstrated success in achieving electrical conductivity in composites fabricated via the incorporation of nanocarbons into various polymer blends, including poly(lactic acid)/polyethylene glycol (PLA/PEG), PLA/poly(lactic-co-glycolic acid) (PLA/PLGA) and poly(methyl methacrylate)/polystyrene (PMMA/PS) [55,67,68]. Additionally, the functionalization of a continuous fibrous network with GO has been used to impart electrical conductivity to a poly(lactic acid)-cotton fiber biocomposites [34].

In the context of this study, steric hindrance arises from the fact that a significant portion of GO lamellae are unable to penetrate the volume occupied by CHS fibers, thus remaining confined to the fiber-matrix interface. These findings suggest that natural fibers serve as a template for GO sheets, which can be thus driven toward the construction of a percolation network even at low loadings, once it is achieved the formation of an interconnected grid of natural fibres.

Indeed, as clearly depicted in the cross-sectional SEM images of cryofractured specimens, reported in **Figure S9**, a robust network of interconnected fibers spans from one side of the specimen to the other, covering the entire cross-section (see red arrows in the micrographs). This distinctive attribute is a direct result of the unique processing technique here adopted, which involves hot pressing to force the macromolecules to infiltrate the interstices within the fiber grid. Remarkably, this method effectively maintains the structural integrity and interconnectivity of the individual fibers, arranged in a layered configuration.

4. Conclusions

A two-step green method was employed to decorate dwarf palm fibers with graphene oxide (GO) nanosheets. Firstly, the lignocellulosic fibers underwent plasma treatment for activation. Subsequently, they were immersed in aqueous suspensions of GO to facilitate the adsorption of nanosheets onto their surface. Two types of GO-coated fiber samples were prepared, differing in the plasma treatment

conditions adopted. These samples were then used to fabricate PBAT-based composites through a hot pressing forced infiltration technique. An appropriate amount of fibers was manually arranged via a hand lay-up process to achieve complete coverage of the mold volume. The fiber arrangement was sandwiched between two PBAT sheets. The resulting composites, containing ca. 50% of fiber loading, were compared with those made using raw fibers, plasma-treated fibers, or GO-coated raw fibers. This comparison aimed to assess the effects of each modification on the properties of the resulting polymer composites. From a mechanical point of view, the various treatments significantly improved the stiffness and resistance of the composites. The combination of plasma treatment and GO coating proved particularly advantageous, resulting in stiffness and tensile strength increments of up to 500% and 300%, respectively. Furthermore, the composites containing GO-coated fibers exhibited electrical conductivity on the order of 10^{-6} S/m. This suggests that the interconnected network of natural fibers can serve as a substrate for the percolation of partially reduced GO sheets.

Funding

This study was carried out within the MICS (Made in Italy – Circular and Sustainable) Extended Partnership and received funding from the European Union Next-GenerationEU (PIANO NAZIONALE DI RIPRESA E RESILIENZA (PNRR) – MISSIONE 4 COMPONENTE 2, INVESTIMENTO 1.3 – D.D. 1551.11-10-2022, PE00000004). This manuscript reflects only the authors' views and opinions, neither the European Union nor the European Commission can be considered responsible for them.

This study was carried out within the SAMOTHRACE (Sicilian micro and nano technology research and innovation center) Extended Partnership and received funding from the European Union Next-GenerationEU (PIANO NAZIONALE DI RIPRESA E RESILIENZA (PNRR) – MISSIONE 4 COMPONENTE 2, INVESTIMENTO 1.5). This manuscript reflects only the authors' views and opinions, neither the European Union nor the European Commission can be considered responsible for them.

References

[1] Scaffaro R, Maio A, Sutera F, Gulino EF, Morreale M. Degradation and recycling of films based on biodegradable polymers: a short review. Polymers (Basel) 2019;11:651. https://doi.org/10.3390/polym11040651.

[2] Naik V, Kumar Mohan , Vijayan V, Kaup a. A Review on Natural Fiber Composite Material in Automotive Applications . Eng Sci 2022;18:1–10. https://doi.org/10.30919/es8d589 .

[3] Devarshi S, Pndhare A, Lokh PE, E E, Mooney JP, S S, et al. Natural Fibre Reinforced Thermoplastic Composite Synthesis Methods and Potential Applications. ES Mater Manuf 2023;21:827. https://doi.org/10.30919/esmm5f827.

[4] Scaffaro R, Maio A, Gulino EF, Megna B. Structure-property relationship of PLA-Opuntia Ficus Indica biocomposites. Compos Part B Eng 2019;167. https://doi.org/10.1016/j.compositesb.2018.12.025.

[5] Scaffaro R, Maio A, Gulino EF, Alaimo G, Morreale M. Green Composites Based on PLA and Agricultural or Marine Waste Prepared by FDM. Polymers (Basel) 2021;13. https://doi.org/10.3390/polym13091361.

[6] Singh N, Singhania RR, Nigam PS, Dong C-D, Patel AK, Puri M. Global status of lignocellulosic biorefinery: Challenges and perspectives. Bioresour Technol 2022;344:126415. https://doi.org/https://doi.org/10.1016/j.biortech.2021.126415.

[7] Mujtaba M, Fernandes Fraceto L, Fazeli M, Mukherjee S, Savassa SM, Araujo de Medeiros G, et al. Lignocellulosic biomass from agricultural waste to the circular economy: a review with focus on biofuels, biocomposites and bioplastics. J Clean Prod 2023;402:136815. https://doi.org/https://doi.org/10.1016/j.jclepro.2023.136815.

[8] An A, Pai P, Kini AK, Ch C, Kini rakant R, B SS. Effect of Natural Fibre-epoxy Plies on the Mechanical and Shock Wave Impact Response of Fibre Metal Laminates . Eng Sci 2022;19:292–300. https://doi.org/10.30919/es8d730 .

[9] Zhubanova A, Abdieva G, Ualieva P, Akimbekov N, Malik A, Tastambek K. Whey-to-Bioethanol Valorisation: Fermentation with Immobilised Yeast Cells . Eng Sci 2024;27:995. https://doi.org/10.30919/es995 .

[10] Yang S, Qu K, Huang Z. Optimizing Hierarchical Porous Carbon from Biomass Waste for High-Performance Supercapacitors . ES Food Agrofor 2022;10:39–50. https://doi.org/10.30919/esfaf803 .

[11] Khan S, Ul-Islam MU, Fatima A, Manan S, Khattak WA, Ullah MW, et al. Potential of Food and Agro-Industrial Wastes for Cost-Effective Bacterial Cellulose Production: An Updated Review of Literature. ES Food Agrofor 2023;13:905. https://doi.org/10.30919/esfaf905.

[12] AlGemayel C, Zeaiter J, Talih S, Saliba NA, Shihadeh A. Mechanistic Analysis of the Pyrolysis of Vegetable Glycerin: A Reactive Force Field-Molecular Dynamics Study. Eng Sci 2023;23:885. https://doi.org/10.30919/es885.

[13] Ghafari R, Scaffaro R, Maio A, Gulino EF, Lo Re G, Jonoobi M. Processing-structure-property relationships of electrospun PLA-PEO membranes reinforced with enzymatic cellulose nanofibers. Polym Test 2020;81. https://doi.org/10.1016/j.polymertesting.2019.106182.

[14] Gao Y, Qu W, Liu Y, Hu H, Cochran E, Bai X. Agricultural residue-derived lignin as the filler of polylactic acid composites and the effect of lignin purity on the composite performance. J Appl Polym Sci 2019;136:47915. https://doi.org/https://doi.org/10.1002/app.47915.

[15] Scaffaro R, Botta L, Lopresti F, Maio A, Sutera F. Polysaccharide nanocrystals as fillers for PLA based nanocomposites. Cellulose 2017;24:447–78. https://doi.org/10.1007/s10570-016-1143-3.

[16] Scaffaro R, Maio A, Gulino EF. Hydrolytic degradation of PLA/Posidonia Oceanica green composites: A simple model based on starting morpho-chemical properties. Compos Sci Technol 2021;213:108930. https://doi.org/https://doi.org/10.1016/j.compscitech.2021.108930.

[17] Huang F, Tian Z, Ma H, Ding Z, Ji X, Si C, et al. Combined alkali impregnation and poly dimethyl diallyl ammonium chloride-assisted cellulase absorption for high-efficiency pretreatment of wheat straw. Adv Compos Hybrid Mater 2023;6. https://doi.org/10.1007/s42114-023-00789-z.

[18] Xu J, Liu R, Wang L, Pranovich A, Hemming J, Dai L, et al. Towards a deep understanding of the biomass fractionation in respect of lignin nanoparticle formation. Adv Compos Hybrid Mater 2023;6:214. https://doi.org/10.1007/s42114-023-00797-z.

[19] Wang F, Wang J, Fang D, Zhou S, Huang J, Zhao G, et al. Surface sizing introducing carbon nanotubes for interfacial bond strengthening of basalt fiber–reinforced polymer composites. Adv Compos Hybrid Mater 2023;6:117. https://doi.org/10.1007/s42114-023-00695-4.

[20] Abbass A, Paiva MC, Oliveira D V, Lourenço PB, Fangueiro R. Graphene/polyurethane nanocomposite coatings – Enhancing the mechanical properties and environmental resistance of natural fibers for masonry retrofitting. Compos Part A Appl Sci Manuf 2023;166:107379. https://doi.org/https://doi.org/10.1016/j.compositesa.2022.107379.

[21] Maio A, Fucarino R, Khatibi R, Rosselli S, Bruno M, Scaffaro R. A novel approach to prevent graphene oxide re-aggregation during the melt compounding with polymers. Compos Sci Technol 2015;119. https://doi.org/10.1016/j.compscitech.2015.10.006.

[22] Chen J, Wu J, Ge H, Zhao D, Liu C, Hong X. Reduced graphene oxide deposited carbon fiber reinforced polymer composites for electromagnetic interference shielding. Compos Part A Appl Sci Manuf 2016;82:141–50. https://doi.org/https://doi.org/10.1016/j.compositesa.2015.12.008.

[23] Qin W, Vautard F, Drzal LT, Yu J. Mechanical and electrical properties of carbon fiber composites with incorporation of graphene nanoplatelets at the fiber–matrix interphase. Compos Part B Eng 2015;69:335–41. https://doi.org/https://doi.org/10.1016/j.compositesb.2014.10.014.

[24] Alemour B, Lim HN, Yaacob MH, Badran O, Hassan MR. Improving the electrical conductivity of carbon fiber reinforced epoxy composite using reduced graphene oxide. Mater Res Express 2019;6:65607. https://doi.org/10.1088/2053-1591/ab0ce5.

[25] Costa UO, Nascimento LFC, Bezerra WBA, Neves PP, Huaman NRC, Monteiro SN, et al. Dynamic and Ballistic Performance of Graphene Oxide Functionalized Curaua Fiber-Reinforced Epoxy Nanocomposites. Polymers (Basel) 2022;14. https://doi.org/10.3390/polym14091859.

[26] Neves PP, Costa UO, Bezerra WBA, Figueiredo AB-H da S, Monteiro SN, Nascimento LFC. Dynamic and Ballistic Performance of Uni- and Bidirectional Pineapple Leaf Fibers (PALF)-Reinforced Epoxy Composites Functionalized with Graphene Oxide. Polymers (Basel) 2022;14. https://doi.org/10.3390/polym14163249.

[27] Sarker F, Karim N, Afroj S, Koncherry V, Novoselov KS, Potluri P. High-Performance Graphene-Based Natural Fiber Composites. ACS Appl Mater Interfaces 2018;10:34502–12. https://doi.org/10.1021/acsami.8b13018.

[28] Zhou S, Zhang C, Xia L, Fu Z, Zhu N, Gong J, et al. A Flexible and Weavable Lignocellulose-Based Photocatalyst Supported by Natural Three-Dimensional Porous Juncus effusus for Highly

Efficient Degradation of Environmental Contaminants. ACS Appl Mater Interfaces 2022;14:27955–67. https://doi.org/10.1021/acsami.2c06207.

[29] Kamatchi T, Saravanan R, Rangappa SM, Siengchin S. Effect of filler content and size on the mechanical properties of graphene-filled natural fiber-based nanocomposites. Biomass Convers Biorefinery 2023. https://doi.org/10.1007/s13399-023-03911-9.

[30] Zhang X, Li J, Gao Q, Wang Z, Ye N, Li J, et al. Nerve-Fiber-Inspired Construction of 3D Graphene "Tracks" Supported by Wood Fibers for Multifunctional Biocomposite with Metal-Level Thermal Conductivity. Adv Funct Mater 2023;33:2213274. https://doi.org/https://doi.org/10.1002/adfm.202213274.

[31] Haikun W, Xiaoshuai H, Lei Q. Recent Progress on the Metacompoistes with Carbonaceous Fillers. Eng Sci 2018;2:17–25. https://doi.org/10.30919/es8d656.

[32] Zhao G, Qian F, Li X, Tang Y, Sheng Y, Li H, et al. Constructing a continuous reduced graphene oxide network in porous plant fiber sponge for highly compressible and sensitive piezoresistive sensors. Adv Compos Hybrid Mater 2023;6:184. https://doi.org/10.1007/s42114-023-00754-w.

[33] Imoisili PE, Adeleke O, Makhatha ME, Jen T-C. Response Surface Methodology (RSM)-Artificial Neural Networks (ANN) Aided Prediction of The Impact Strength of Natural Fibre/Carbon Nanotubes Hybrid Reinforced Polymer Nanocomposite . Eng Sci 2023;23:852. https://doi.org/10.30919/es8d852 .

[34] He Y, Wu S, Yuen ACY, Huang F, Boyer C, Wang CH, et al. Scalable Manufacturing Process and Multifunctional Performance of Cotton Fibre-Reinforced Poly(Lactic Acid) (PLA) Bio-Composites Coated by Graphene Oxide. Polymers (Basel) 2022;14. https://doi.org/10.3390/polym14193946.

[35] Scaffaro R, Maio A, Lopresti F, Botta L. Nanocarbons in electrospun polymeric nanomats for tissue engineering: A review. Polymers (Basel) 2017;9. https://doi.org/10.3390/polym9020076.

[36] Maio A, Pibiri I, Morreale M, Mantia FP La, Scaffaro R. An Overview of Functionalized Graphene Nanomaterials for Advanced Applications. Nanomaterials 2021;11. https://doi.org/10.3390/nano11071717.

[37] Li F, Bi Z, Kimura H, Li H, Liu L, Xie X, et al. Energy- and cost-efficient salt-assisted synthesis of nitrogen-doped porous carbon matrix decorated with nickel nanoparticles for superior electromagnetic wave absorption. Adv Compos Hybrid Mater 2023;6:133. https://doi.org/10.1007/s42114-023-00710-8.

[38] Huang A, Guo Y, Zhu Y, Chen T, Yang Z, Song Y, et al. Durable washable wearable antibacterial thermoplastic polyurethane/carbon nanotube@silver nanoparticles electrospun membrane strain sensors by multi-conductive network. Adv Compos Hybrid Mater 2023;6:101. https://doi.org/10.1007/s42114-023-00684-7.

[39] Xu Q, Wu Z, Zhao W, He M, Guo N, Weng L, et al. Strategies in the preparation of conductive polyvinyl alcohol hydrogels for applications in flexible strain sensors, flexible supercapacitors, and triboelectric nanogenerator sensors: an overview. Adv Compos Hybrid Mater 2023;6:203. https://doi.org/10.1007/s42114-023-00783-5.

[40] Cao X, Lan D, Zhang Y, Jia Z, Wu G, Yin P. Construction of three-dimensional conductive network and heterogeneous interfaces via different ratio for tunable microwave absorption. Adv Compos Hybrid Mater 2023;6:187. https://doi.org/10.1007/s42114-023-00763-9.

[41] Cheng K, Zou L, Chang B, Liu X, Shi H, Li T, et al. Mechanically robust and conductive poly(acrylamide) nanocomposite hydrogel by the synergistic effect of vinyl hybrid silica nanoparticle and polypyrrole for human motion sensing. Adv Compos Hybrid Mater 2022;5:2834–46. https://doi.org/10.1007/s42114-022-00465-8.

[42] Cao G, Cai S, Zhang H, Tian Y. High-performance conductive adhesives based on water-soluble resins for printed circuits, flexible conductive films, and electromagnetic interference shielding devices. Adv Compos Hybrid Mater 2022;5:1730–42. https://doi.org/10.1007/s42114-021-00402-1.

[43] Chen J, Zhu Y, Chang X, Pan D, Song G, Guo Z, et al. Recent Progress in Essential Functions of Soft Electronic Skin. Adv Funct Mater 2021;31:2104686. https://doi.org/https://doi.org/10.1002/adfm.202104686.

[44] Wu Y, Chen E, Weng X, He Z, Chang G, Pan X, et al. Conductive Polyvinyl Alcohol/Silver Nanoparticles Hydrogel Sensor with Large Draw Ratio, High Sensitivity and High Stability for

Human Behavior Monitoring. Eng Sci 2022;18:113–20. https://doi.org/10.30919/es8d659.

[45] Shi Y, Li B, Jiang X, Yu C, Li T, Sun H, et al. In situ enhancing thermal and mechanical properties of novel green WPAI nanocomposite membrane via artificially cultivated biomass-based diatom frustules. Adv Compos Hybrid Mater 2023;6:36. https://doi.org/10.1007/s42114-022-00621-0.

[46] Scaffaro R, Maio A, Gammino M. Electrospun polymeric nanohybrids with outstanding pollutants adsorption and electroactivity for water treatment and sensing devices. Adv Compos Hybrid Mater 2024;7:13. https://doi.org/10.1007/s42114-023-00827-w.

[47] Khan F, Ahmad SR, Kronfli E. γ-Radiation Induced Changes in the Physical and Chemical Properties of Lignocellulose. Biomacromolecules 2006;7:2303–9. https://doi.org/10.1021/bm060168y.

[48] Koohestani B, Darban AK, Mokhtari P, Yilmaz E, Darezereshki E. Comparison of different natural fiber treatments: a literature review. Int J Environ Sci Technol 2019;16:629–42. https://doi.org/10.1007/s13762-018-1890-9.

[49] de Farias JGG, Cavalcante RC, Canabarro BR, Viana HM, Scholz S, Simão RA. Surface lignin removal on coir fibers by plasma treatment for improved adhesion in thermoplastic starch composites. Carbohydr Polym 2017;165:429–36. https://doi.org/https://doi.org/10.1016/j.carbpol.2017.02.042.

[50] Zhang H, Yu J, Wang J. Non-Thermal Oxygen-Helium Plasma Modification and Regeneration of Sawdust Biochar to Promote Aniline Removal . ES Energy Environ 2022;15:15–27. https://doi.org/10.30919/esee8c601 .

[51] Fan G, Wang Z, Ren H, Liu Y, Fan R. Dielectric dispersion of copper/rutile cermets: Dielectric resonance, relaxation, and plasma oscillation. Scr Mater 2021;190:1–6. https://doi.org/https://doi.org/10.1016/j.scriptamat.2020.08.027.

[52] Yuan X, Jayaraman K, Bhattacharyya D. Plasma treatment of sisal fibres and its effects on tensile strength and interfacial bonding . J Adhes Sci Technol 2002;16:703–27. https://doi.org/10.1163/156856102760099898.

[53] Gupta US, Dhamarikar M, Dharkar A, Chaturvedi S, Kumrawat A, Giri N, et al. Plasma modification of natural fiber: A review. Mater Today Proc 2021;43:451–7. https://doi.org/https://doi.org/10.1016/j.matpr.2020.11.973.

[54] Scaffaro R, Maio A, Gammino M, Alaimo G. Modelling the structure-property relationships of high performance PBAT-based biocomposites with natural fibers obtained from Chamaerops humilis dwarf palm. Compos Sci Technol 2022;223:109427. https://doi.org/https://doi.org/10.1016/j.compscitech.2022.109427.

[55] Scaffaro R, Maio A, Lo Re G, Parisi A, Busacca A. Advanced piezoresistive sensor achieved by amphiphilic nanointerfaces of graphene oxide and biodegradable polymer blends. Compos Sci Technol 2018;156:166–76. https://doi.org/https://doi.org/10.1016/j.compscitech.2018.01.008.

[56] Scaffaro R, Maio A. Influence of oxidation level of graphene oxide on the mechanical performance and photo-oxidation resistance of a polyamide 6. Polymers (Basel) 2019;11. https://doi.org/10.3390/polym11050857.

[57] Maio A, Gammino M, Fortunato Gulino E, Megna B, Fara P, Scaffaro R. Rapid One-Step Fabrication of Graphene Oxide-Decorated Polycaprolactone Three-Dimensional Templates for Water Treatment. ACS Appl Polym Mater 2020;2:4993–5005. https://doi.org/10.1021/acsapm.0c00852.

[58] Scaffaro R, Gammino M, Maio A. Wet electrospinning-aided self-assembly of multifunctional GO-CNT@PCL core-shell nanocomposites with spider leg bioinspired hierarchical architectures. Compos Sci Technol 2022;221:109363. https://doi.org/https://doi.org/10.1016/j.compscitech.2022.109363.

[59] Scaffaro R, Maio A, Gammino M. Hybrid biocomposites based on polylactic acid and natural fillers from Chamaerops humilis dwarf palm and Posidonia oceanica leaves. Adv Compos Hybrid Mater 2022;5:1988–2001. https://doi.org/10.1007/s42114-022-00534-y.

[60] Sun D, Hussain HI, Yi Z, Siegele R, Cresswell T, Kong L, et al. Uptake and cellular distribution, in four plant species, of fluorescently labeled mesoporous silica nanoparticles. Plant Cell Rep 2014;33:1389–402. https://doi.org/10.1007/s00299-014-1624-5.

[61] Dimiev AM, Shukhina K, Khannanov A. Mechanism of the graphene oxide formation: The role

of water, “reversibility” of the oxidation, and mobility of the C–O bonds. Carbon N Y 2020;166:1–14. https://doi.org/https://doi.org/10.1016/j.carbon.2020.05.005.

[62] Lazorenko G, Kasprzhitskii A, Yavna V, Mischinenko V, Kukharskii A, Kruglikov A, et al. Effect of pre-treatment of flax tows on mechanical properties and microstructure of natural fiber reinforced geopolymer composites. Environ Technol Innov 2020;20:101105. https://doi.org/https://doi.org/10.1016/j.eti.2020.101105.

[63] Geminiani L, Campione FP, Corti C, Luraschi M, Motella S, Recchia S, et al. Differentiating between Natural and Modified Cellulosic Fibres Using ATR-FTIR Spectroscopy. Heritage 2022;5:4114–39. https://doi.org/10.3390/heritage5040213.

[64] Maio A, Giallombardo D, Scaffaro R, Palumbo Piccionello A, Pibiri I. Synthesis of a fluorinated graphene oxide-silica nanohybrid: Improving oxygen affinity. RSC Adv 2016;6. https://doi.org/10.1039/c6ra02585d.

[65] Wang Z, Nelson JK, Hillborg H, Zhao S, Schadler LS. Nonlinear conductivity and dielectric response of graphene oxide filled silicone rubber nanocomposites. 2012 Annu. Rep. Conf. Electr. Insul. Dielectr. Phenom., 2012, p. 40–3. https://doi.org/10.1109/CEIDP.2012.6378717.

[66] Wang Z, Nelson JK, Hillborg H, Zhao S, Schadler LS. Graphene Oxide Filled Nanocomposite with Novel Electrical and Dielectric Properties. Adv Mater 2012;24:3134–7. https://doi.org/https://doi.org/10.1002/adma.201200827.

[67] Kiran Raj G, Singh E, Hani U, Ramesh KVRNS, Talath S, Garg A, et al. Conductive polymers and composites-based systems: An incipient stride in drug delivery and therapeutics realm. J Control Release 2023;355:709–29. https://doi.org/https://doi.org/10.1016/j.jconrel.2023.02.017.

[68] Mao C, Zhu Y, Jiang W. Design of Electrical Conductive Composites: Tuning the Morphology to Improve the Electrical Properties of Graphene Filled Immiscible Polymer Blends. ACS Appl Mater Interfaces 2012;4:5281–6. https://doi.org/10.1021/am301230q.

Figures

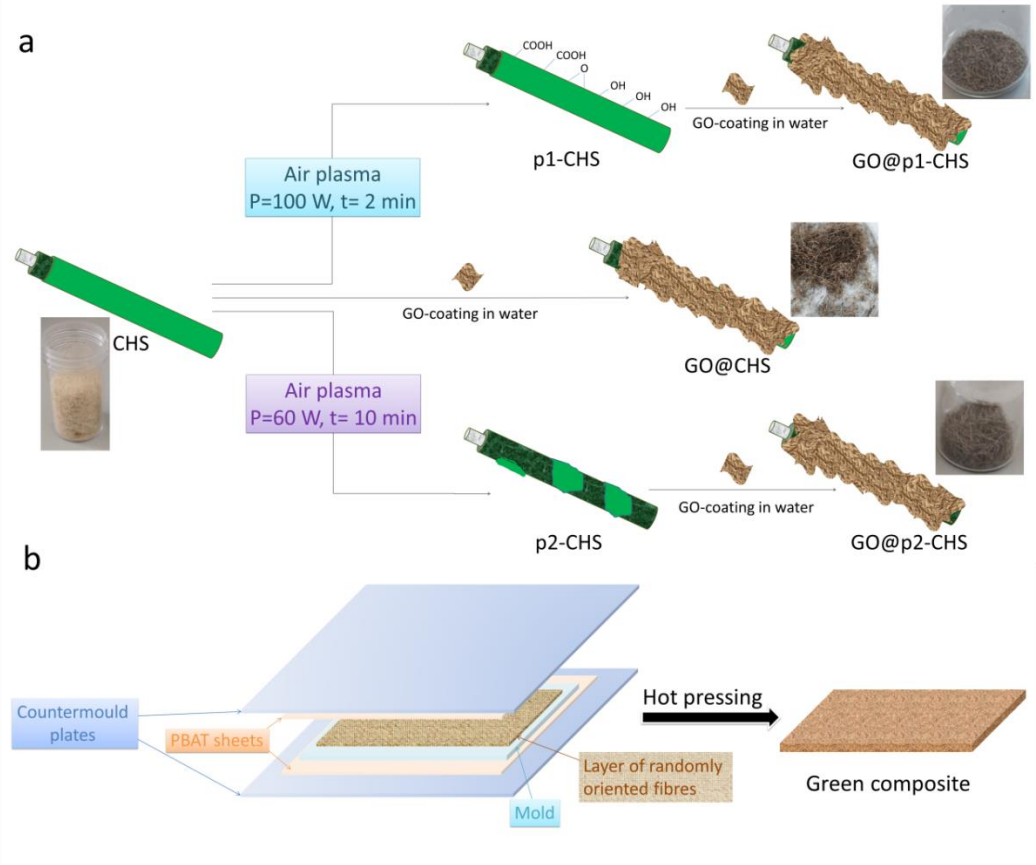

Figure 1. Schematics of the pathways followed to achieve GO-coated CHS fibres (a) and green composites (b). Digital photographs of the various samples provide the visual inspection of fibers before and after GO-coating to highlight the color change from light brown to grey after coating.

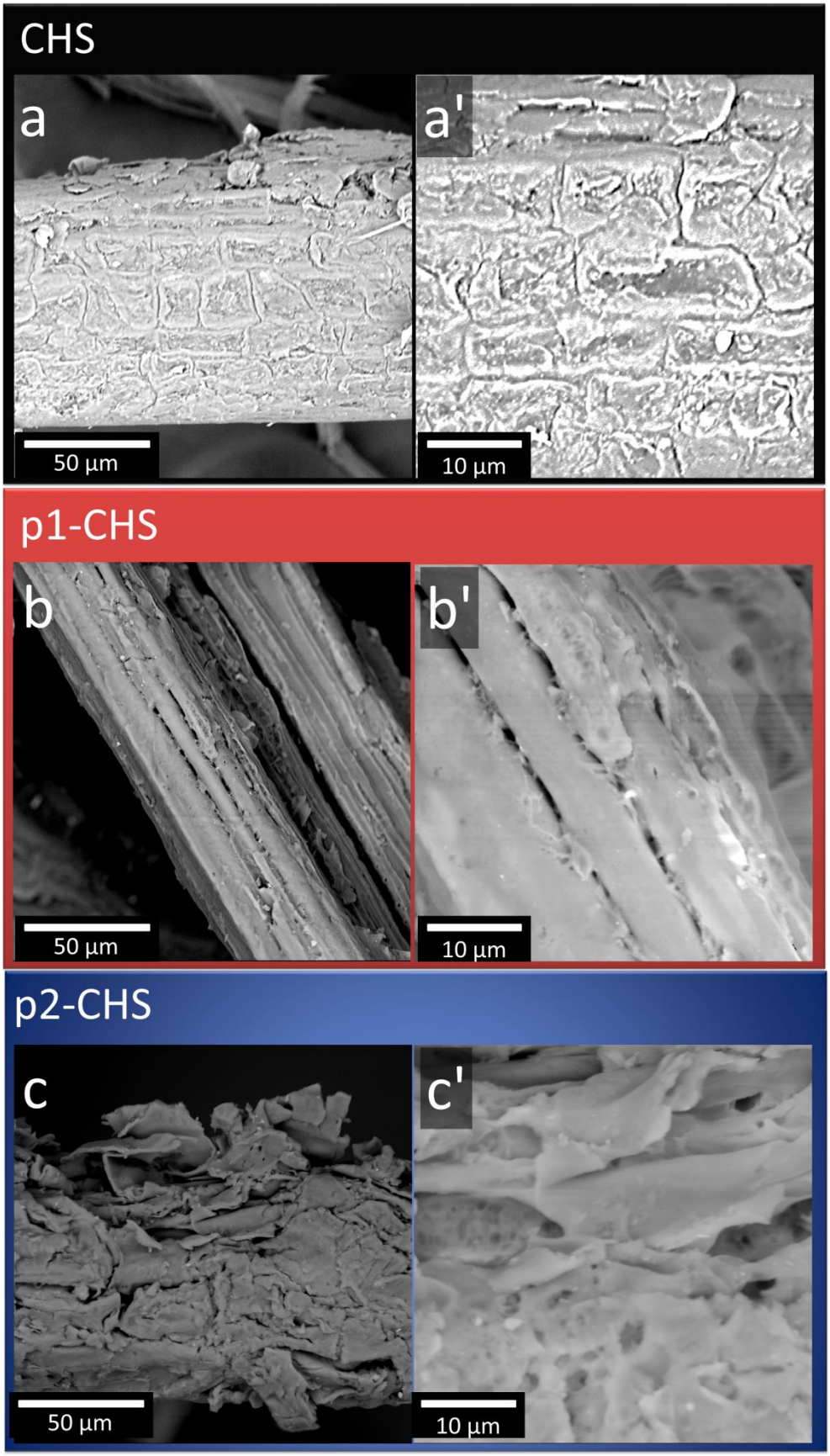

Figure 2. SEM micrographs of raw CHS (a-a'), p1-CHS (b-b'), p2-CHS (c-c') at different magnifications.

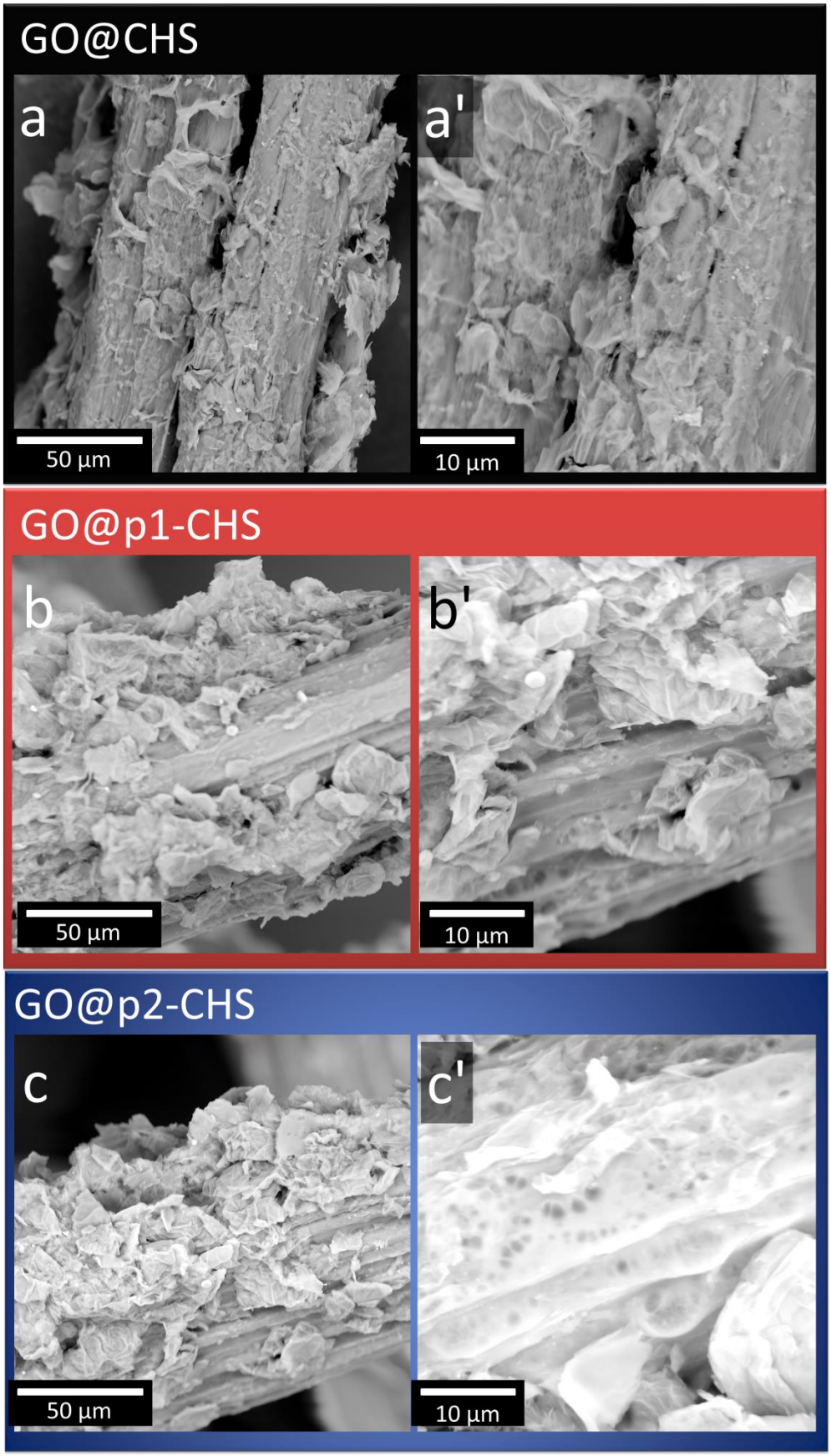

Figure 3. SEM micrographs of GO@CHS (a-a'), GO@p1-CHS (b-b'), GO@p2-CHS (c-c') at different magnifications.

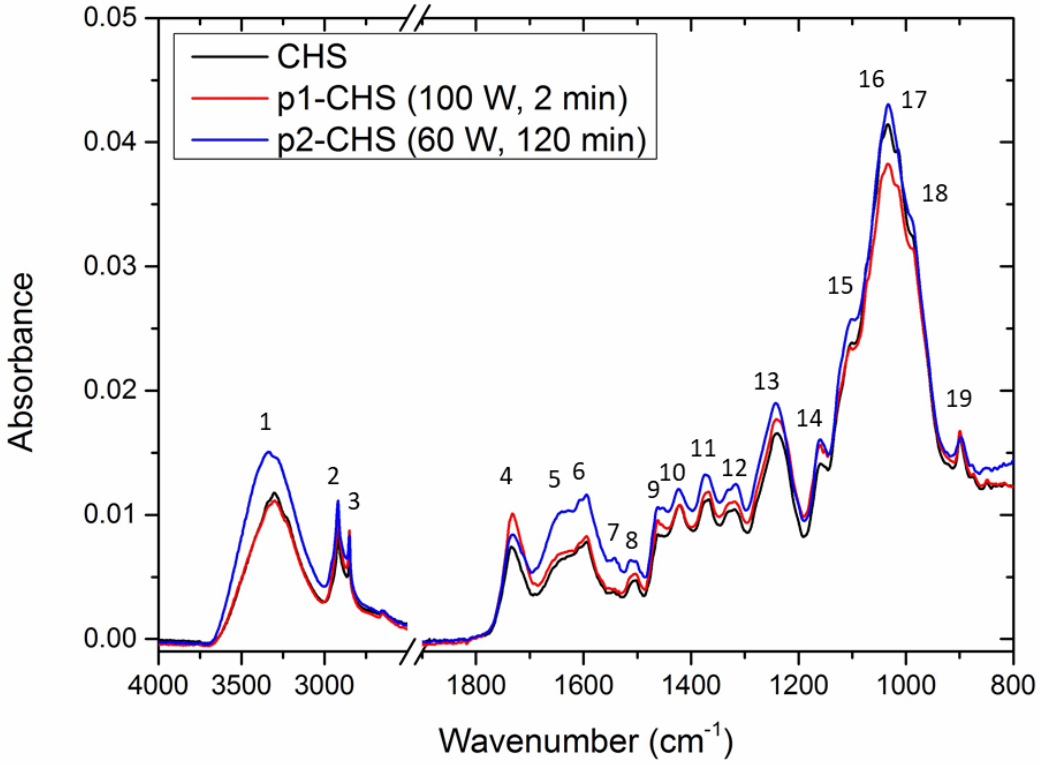

Figure 4. FTIR/ATR spectra collected in the range 4000-800 cm^{-1} for raw and plasma-treated CHS fibres (for interpretation of the references to color in this figure legend, the reader is referred to the web version of this article).

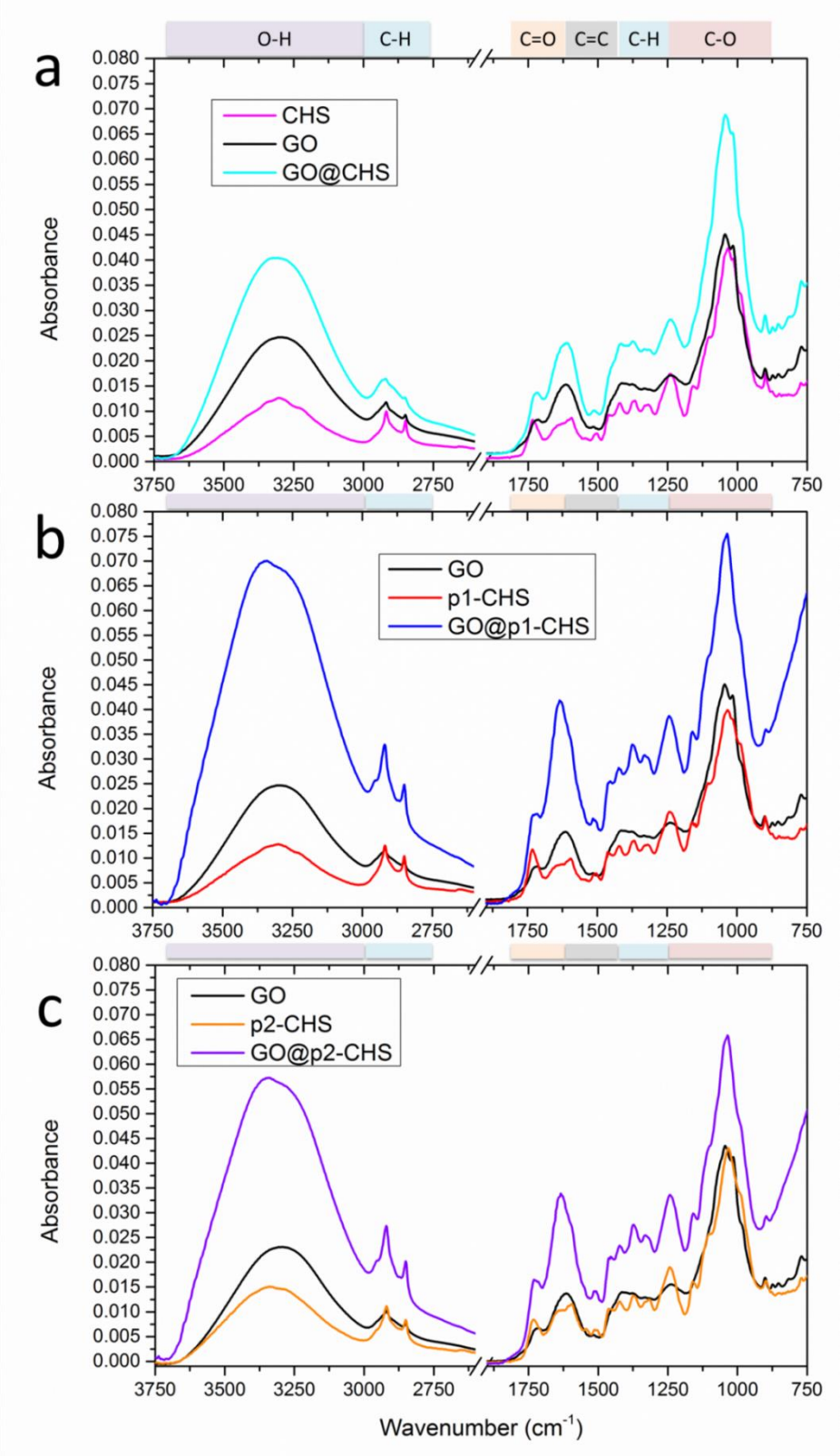

Figure 5. FTIR/ATR spectra of CHS (a), p1-CHS (b), and p2-CHS fibres (c) before and after coating with GO, together with spectrum of GO as a reference (for interpretation of the references to color in this figure legend, the reader is referred to the web version of this article).

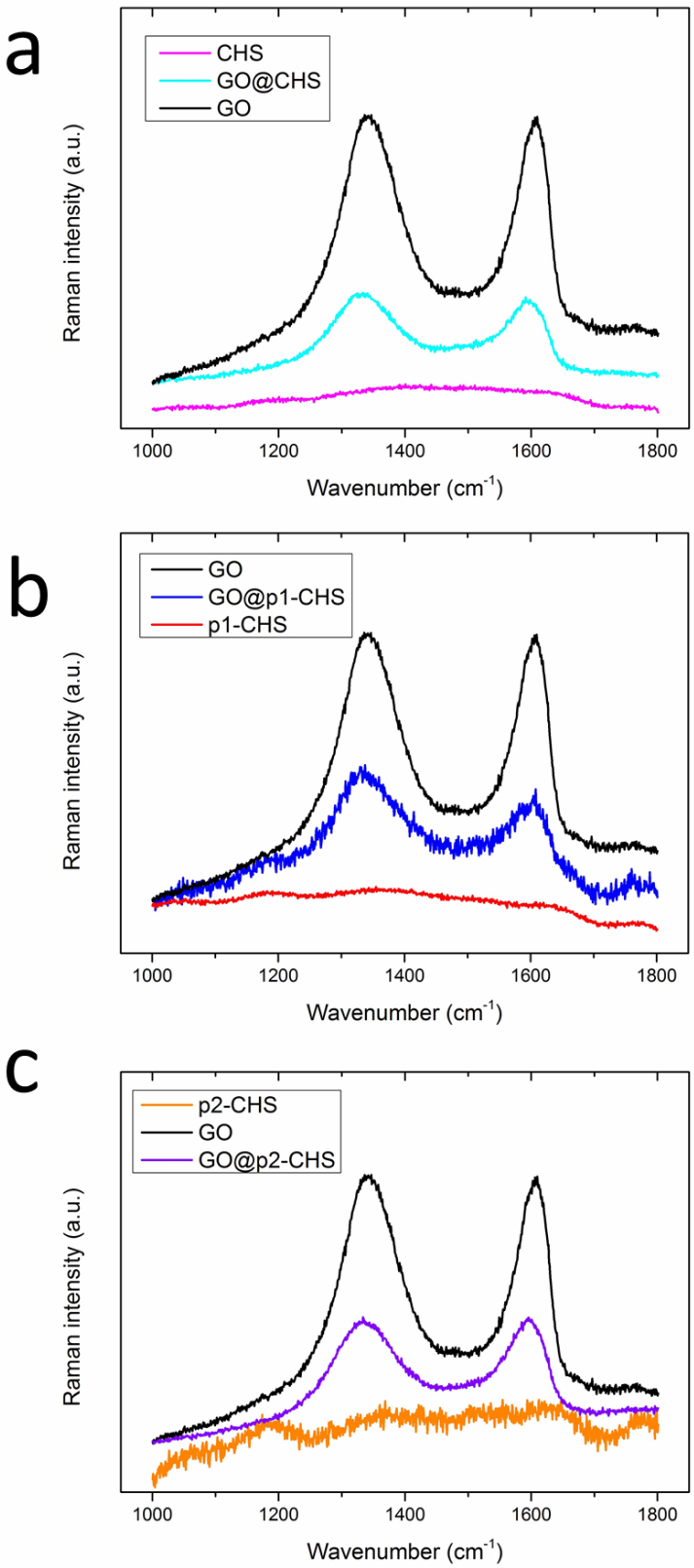

Figure 6. Micro-Raman spectra of CHS (a), p1-CHS (b), and p2-CHS fibres (c) before and after coating with GO, together with spectrum of GO as a reference (for interpretation of the references to colours in this figure legend, the reader is referred to the web version of this article).

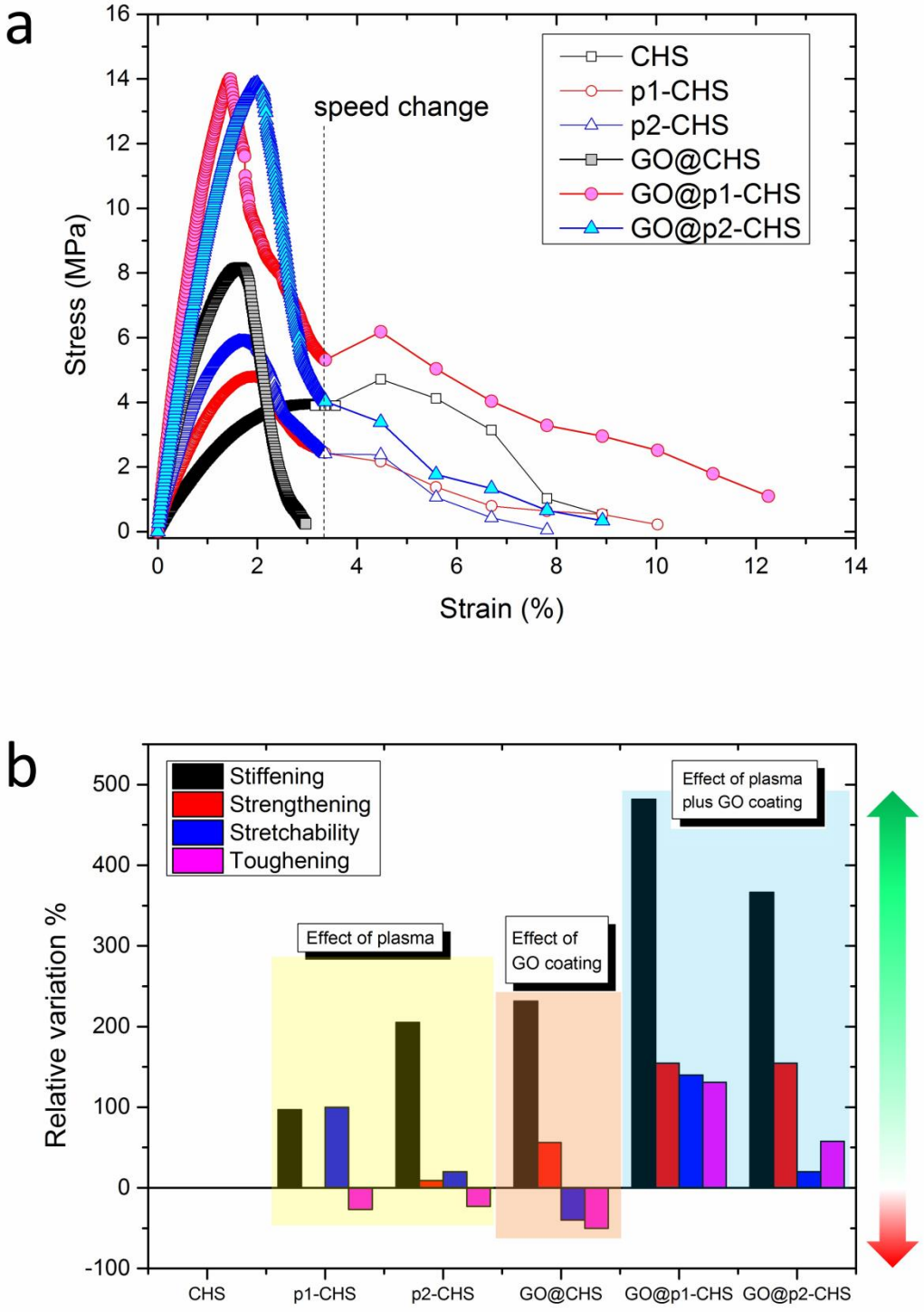

Figure 7. Representative stress-strain curves of the green composites containing 50 wt.% of fibers (a) and synoptic overview of relative variations observed in the elastic modulus (stiffening), tensile strength (strengthening), elongation at break (stretchability) and toughness (toughening) of composites after each treatment (b).

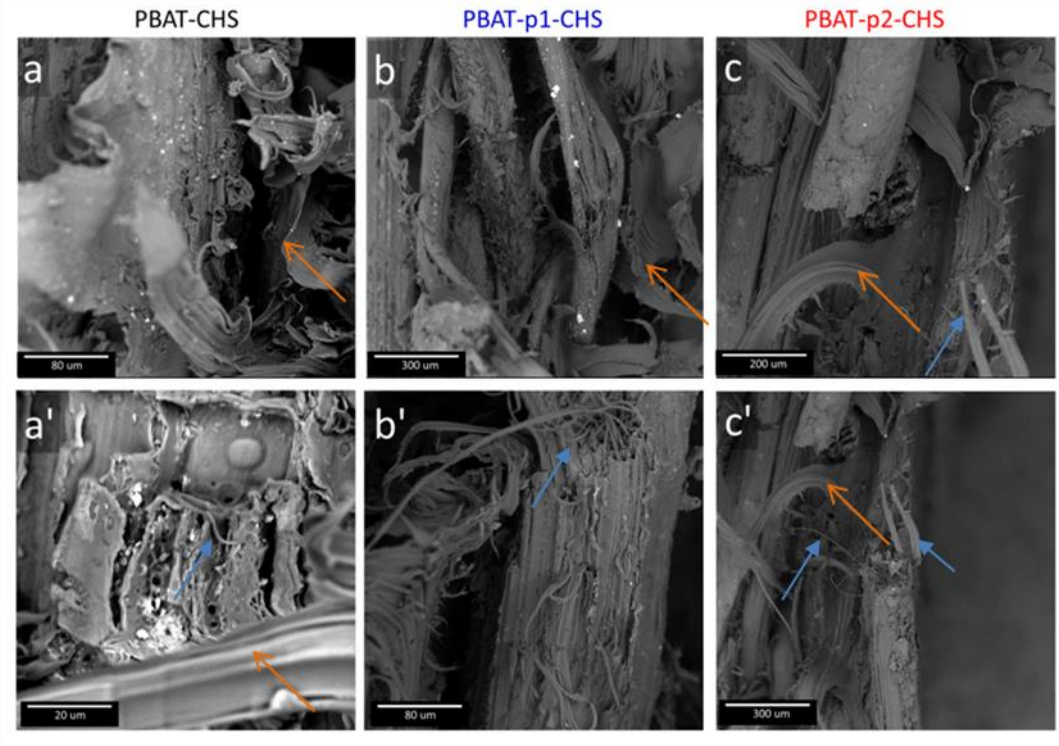

Figure 8. SEM micrographs of PBAT composites containing CHS (a-a'), p1-CHS (b-b'), and p2-CHS (c-c') after tensile failure, acquired in two different specimen positions for each sample. Orange arrows (V-shaped arrowhead) indicate deformed PBAT phase, blue arrows (triangular shaped arrowhead) indicate fraying events with defibrillation (for interpretation of the references to color in this figure, the reader is referred to the web version of this article).

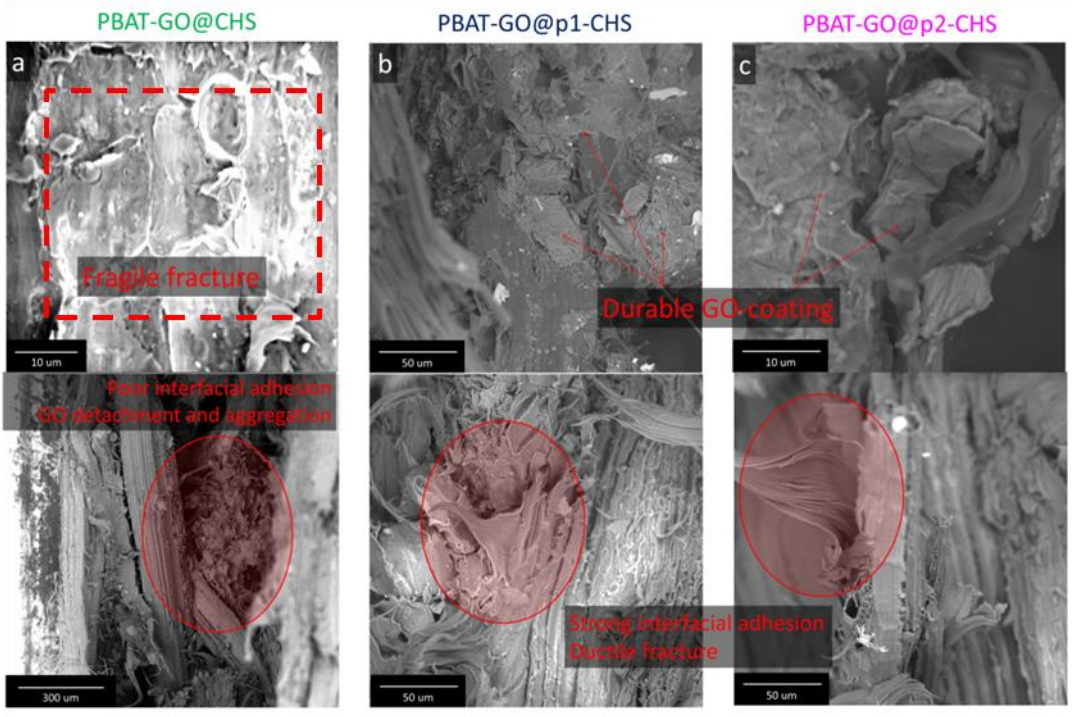

Figure 9. SEM micrographs of PBAT composites containing GO@CHS (a), GO@p1-CHS (b), and GO@p2-CHS (c) after tensile failure, acquired in two different specimen positions for each sample. Red dashed area and circle in (a) highlights the fragile area of fracture and the detachment of GO from fibers and the fiber-matrix debonding, respectively; red circles in (b-c) put into evidence the polymer phase deformed yet still adherent to fiber surface, symptomatic of strong interfacial adhesion and ductile mode of failure.

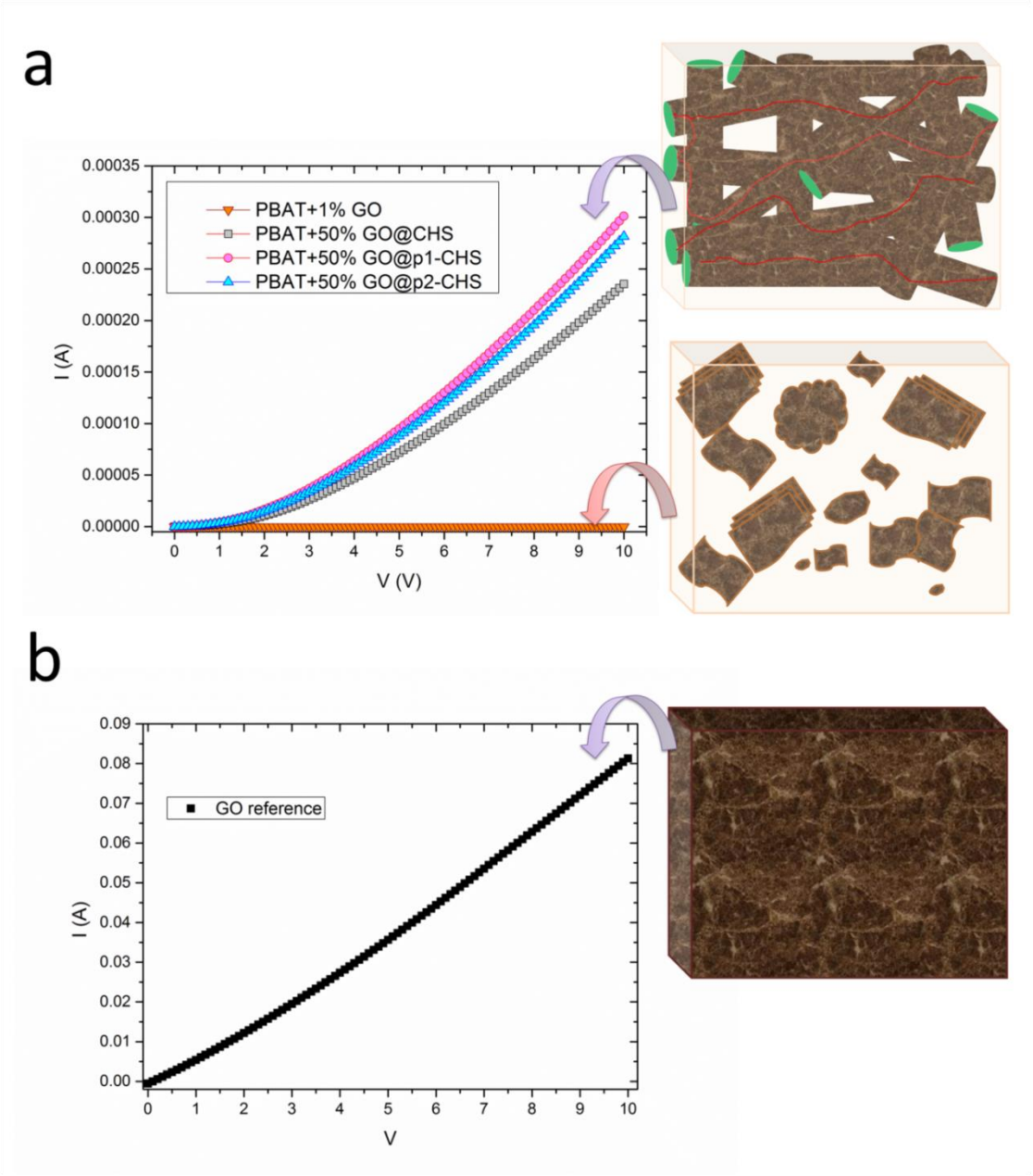

Figure 10. I-V curves of the green composites compared to that of a PBAT loaded with the equivalent GO content (PBAT+1% GO); I-V characteristics of a specimen made of GO thermally treated in the same way as composites (b).

Tables

Table 1. Main FTIR/ATR band assignments [49,62,63]

#	Wavenumber (cm^{-1})	Assignment	Component of CHS fiber
1	3273	OH stretching	Hemicellulose, cellulose
2	2916	C-H asymmetric stretching	Hemicellulose, cellulose
3	2849	C-H symmetric stretching	Hemicellulose, cellulose
4	1733	C=O stretching	Hemicellulose, pectin, lignin
5	1634	C=O stretching/OH bending	Water, hemicellulose
6	1594	C=C stretching	Lignin
7	1540	$-COO^-$ or N-H vibration stretching	Emergent after p2-treatment
8	1508	C=O stretching conjugated to aromatic ring	Lignin
9	1461	Asymmetric bending of CH_3 in methoxyl groups	Lignin
10	1422	CH_2 scissoring deformation/vibrations of aromatic structure	Lignin
11	1368	C-H bending deformation	Cellulose, lignin
12	1317	$-CH_2$ in plane-angular vibration	Cellulose (crystalline)
13	1239	C-O stretching of acetyl group	Hemicellulose and lignin
14	1159	C-O-C asymmetric stretching	Cellulose and hemicellulose
15	1103	C-O asymmetric in-plane stretching	Cellulose and hemicellulose
16	1049	C-O stretching	Cellulose
17	1025	C-O stretching	Cellulose
18	982	C-O stretching and ring vibrational modes	Cellulose
19	897	β-glycosidic linkage	Cellulose (crystalline and amorphous)

Table 2. GO content of the three samples of CHS fibres

Sample	GO@CHS	p1-CHS	p2-CHS
GO (wt.%)	1.68	2.12	1.96

Table 3. Salient mechanical properties of composites recorded during tensile tests

	PBAT+50% CHS	PBAT+50% p1-CHS	PBAT+50% p2-CHS	PBAT+50% GO@CHS	PBAT+50% GO@p1-CHS	PBAT+50% GO@p2-CHS
E (MPa)	270±21	532±28	824±35	895±43	1571±55	1260 ±48
TS (MPa)	5.5±0.2	5.5±0.3	6±0.2	8.6±0.2	14 ±0.1	14 ±0.2
EB (%)	5±2	10±1	6±2	3±0.01	12±2	6±2
k (MJ/m^3)	0.26±0.011	0.19±0.01	0.20±0.01	0.13±0.001	0.60±0.011	0.41±0.013

Table 4. Porosity of the composites investigated

Sample	PBAT+50% CHS	PBAT+50% p1-CHS	PBAT+50% p2-CHS	PBAT+50% GO@CHS	PBAT+50% GO@p1-CHS	PBAT+50% GO@p2-CHS
Porosity (%)	15	15	10	16	21	19

Table 5. Electrical conductivity of the samples

Sample	Electrical conductivity (S/m)
GO	1.13E-03
PBAT	ND
PBAT+1%GO	1.5810E-11
PBAT+CHS	ND
PBAT+p1-CHS	ND
PBAT+p2-CHS	ND
PBAT+GO@CHS	1.99E-06
PBAT+GO@p1-CHS	2.63E-06
PBAT+GO@p2-CHS	2.45E-06